Molecular-engineered biradicals based on the Y III -phthalocyanine platform

Nithin Suryadevara, Athanassios Boudalis, Jorge Enrique Olivares Peña, Eufemio Moreno-Pineda, Artem Fediai, Wolfgang Wenzel, Philippe Turek, Mario Ruben

Molecular-engineered biradicals based on the Y^{III}-phthalocyanine platform

Nithin Suryadevara,[a,b] Athanassios K. Boudalis,*[b,c,e] Jorge Enrique Olivares Peña,[a] Eufemio Moreno-Pineda,*[d] Artem Fediai,[a] Wolfgang Wenzel,[a] Philippe Turek,[e] Mario Ruben*[a,b,c]

[a]*Institute of Nanotechnology (INT), Karlsruhe Institute of Technology (KIT), D-76344 Eggenstein-Leopoldshafen, Germany. E-mail: mario.ruben@kit.edu*
[b]*Institute for Quantum Materials and Technology (IQMT), Karlsruhe Institute of Technology (KIT), D-76344 Eggenstein-Leopoldshafen, Germany. E-mail: bountalis@kit.edu*
[c]*Institut de Science et d'Ingénierie Suparamolaiculaires – ISIS, 8 allée Gaspard Monge, BP 70028, F-67083 Strasbourg Cedex, France. E-mail: bountalis@unistra.fr*
[d]*Departamento de Química-Física, Escuela de Química, Facultad de Ciencias Naturales, Exactas y Tecnología, Universidad de Panamá, Panamá.*
[e]*Institut de Chimie de Strasbourg (UMR 7177, CNRS-Unistra), Université de Strasbourg, 4 rue Blaise Pascal, CS 90032, F-67081 Strasbourg, France.*

1 Abstract

A mixed-ligand phthalocyanine/porphyrin yttrium(III) radical double-decker complex (**DD**) was synthesized using the custom-made 5,10,15-tris(4-methoxyphenyl)-20-(4-((trimethylsilyl)ethynyl)phenyl)porphyrin. The trimethylsilyl functionality was then used to couple two such complexes into biradicals through rigid tethers. Glaser coupling was used to synthesize a short-tethered biradical (**C1**) and Sonogashira coupling to synthesize longer-tethered ones (**C2**, **C3**). Field-swept echo-detected (FSED), saturation recovery and spin nutation pulsed EPR experiments revealed marked similarities of the magnetic properties of **DD** with those of the parent $[Y(pc)_2]^{\cdot}$ complex, both in the solid state and in $CD_2Cl_2/CDCl_3$ 4:1 frozen glasses. FSED experiments on the biradicals **C2** and **C3** revealed a spectral broadening with respect to the spectra of **DD** and $[Y(pc)_2]^{\cdot}$ assigned to the effect of dipolar interactions in solution. Apart from the main resonance, satellite features were also observed, which were simulated with dipole-dipole pairs of shortest distances, suggesting spin delocalization on the organic tether. FSED experiments on **C1** yielded spectral line shapes that could not be simulated, as the integration of the off-resonance echoes was complicated by field-dependent modulations. While for all dimers the on-resonance spin nutation experiments yielded Rabi oscillations of the same frequencies, off-resonance nutations on **C1** yielded Rabi oscillations that could be assigned to a $M_S = -1$ to $M_S = 0$ transition within an $S = 1$ multiplet. DFT calculations showed that the *trans* conformation of the complexes was significantly more stable than the *cis* one and that it induced a marked spin delocalization over the rigid organic tether. This "spin leakage" was most pronounced for the shortest biradical **C1**.

2 Introduction

Molecular spin qubits constitute an intensely investigated area of spintronic applications, with a major advantage the ability to fine-tune their structures and magnetic properties by synthetic means, such as molecular engineering. Indeed, using phthalocyanine lanthanide(III) complexes as a launchpad, we have previously been able to construct molecular spin transistors using the Single-Molecule Magnet $[Tb(pc)_2]^{\cdot}$ where the nuclear spin states were read-out electrically[1] and subsequently used to implement the Grover's algorithm.[2]

Mindful of the fact that the large Hilbert spaces of these molecules are useful for the construction of qu*d*its, a strategy toward this goal has been based upon the ability of such complexes to form triple or quadruple-decker complexes.[3–8] In these systems, (mainly) dipolar interactions between Tb^{III} ions are expected to create a Hilbert space of increased dimensions, thereby achieving the goal of qu*d*it construction.

However, this approach rests upon the stability of these multidecker architectures and on their serendipitous assembly. Moreover, it gives access to very narrow range of dipolar interaction strengths, since the intermetallic distances cannot be tuned at will.

A different approach was proposed by Yamashota and Kato based on a fused-Pc ligand. In that case, the fused bis-phthalocyanine is shared between two {Tb(pc)} moieties, acting as a rigid bridge between them.[9] While this approach still offers a fixed distance between the metal centres, conceptually it allows us to envision shared ligands of variable lengths, modulating the distance of the bridged complexes.

We were therefore interested in developing an alternative method based on molecular engineering principles that would give access to well-defined and stable architectures, easily tunable intermetallic distances and predictable preparatory pathways. Our goal was then to connect such mononuclear entities with long organic tethers through which dipolar interactions of controlled strength could be achieved.

Given the availability of mixed-ligand phthalocyanine/porphyrin Ln^{III} complexes,[10,11] we considered that this goal could be best achieved by taking advantage of the higher synthetic versatility offered by the *meso*-position carbons of porphyrins. We therefore focused on designing and synthesizing bis-porphyrinato ligands to serve as bridges between {Tb(pc)} moieties.

From a magnetic perspective though, it was crucial that we first determine whether the magnetic properties of the $[Tb(pc)_2]^{\cdot}$ platform would be retained upon replacement of one of the $pc^{0/-}$ ligands with a $por^{0/-}$ one, including the spin density distribution over the two ligands, which could no longer be considered as strictly equivalent. Subsequently, we needed to assess the spin density distributions and magnetic behaviors of such biradical of mixed-ligand systems, and whether the point-dipole approximation could be regarded as valid.

However, these systems are complicated by the simultaneous presence of the Tb^{III} electron spin alongside that of the delocalized radical system, rendering detailed analyses significantly more difficult. A strategy to counter this complication was tackling this system in an incremental manner, by replacing the paramagnetic Tb^{III} by the diamagnetic Y^{III} ion, thus greatly simplifying the problem. This approach was further indicated by the tendency we discovered for these supramolecular systems (see below) not to form crystalline solids, thus precluding previously used characterization methods, such as micro-SQUID magnetometry. Instead, replacement of

Tb^{III} by Y^{III} allowed us to use EPR spectroscopy, which is particularly powerful to answer such questions.

As a first step of this project, we carried out EPR studies of pure $[Y(pc)_2]^{\cdot}$ in the solid state. These demonstrated that magnetically condensed and non-isotopically engineered phases could be coherently manipulated even at room temperatures, as demonstrated by FID-detected Rabi oscillations. Theoretical studies also demonstrated a preponderance of spin densities on carbon atoms of the pc rings, partially explaining the absence of hyperfine interactions.[12]

In this work, to better understand the spin-density distributions in molecular-engineered quantum systems based on phthalocyanine radicals, we present detailed continuous-wave/pulsed EPR studies of such tailored-designed biradical systems in the solid state and in solution, which we rationalize through DFT calculations. Whenever required, we also present relevant studies on the parent $[Y(pc)_2]^{\cdot}$ system, reported for the first time in this work, to demonstrate the retention of its properties in the newly reported molecular-engineered systems.

3 Results

3.1 Syntheses

In order to design and build the polynuclear architectures, we require several elements that include the building block, the linker, and the mechanism to couple them. Here, in our case, we chose the porphyrin and phthalocyanine based double-decker as a building block and coupling reactions as a linking strategy. The scheme below shows a clear view of the synthesis, which requires a single sandwich complex and thus can synthesize a family of coupled double-decker complexes, just by varying the linkers and reaction conditions.

The neutral forms of the couple dimeric sandwich complexes (**C1-C3**) were synthesized using Glaser and Sonogashira coupling from the mononuclear double-decker complex **DD**, as depicted in Figure 1. In order to obtain the dimeric complex **C1**, the homo-coupling mechanism was involved in the presence of $Pd(PPh_3)_2Cl$, $AsPPh_3$ in aerobic conditions. The oxygen favors the mechanism of the homo-coupling reaction. Whereas in the case of synthesis of complexes **C2** and **C3**, the mono-nuclear complex **DD** was involved in hetero-coupling with a linker, but with inert conditions for the Sonogashira reaction.

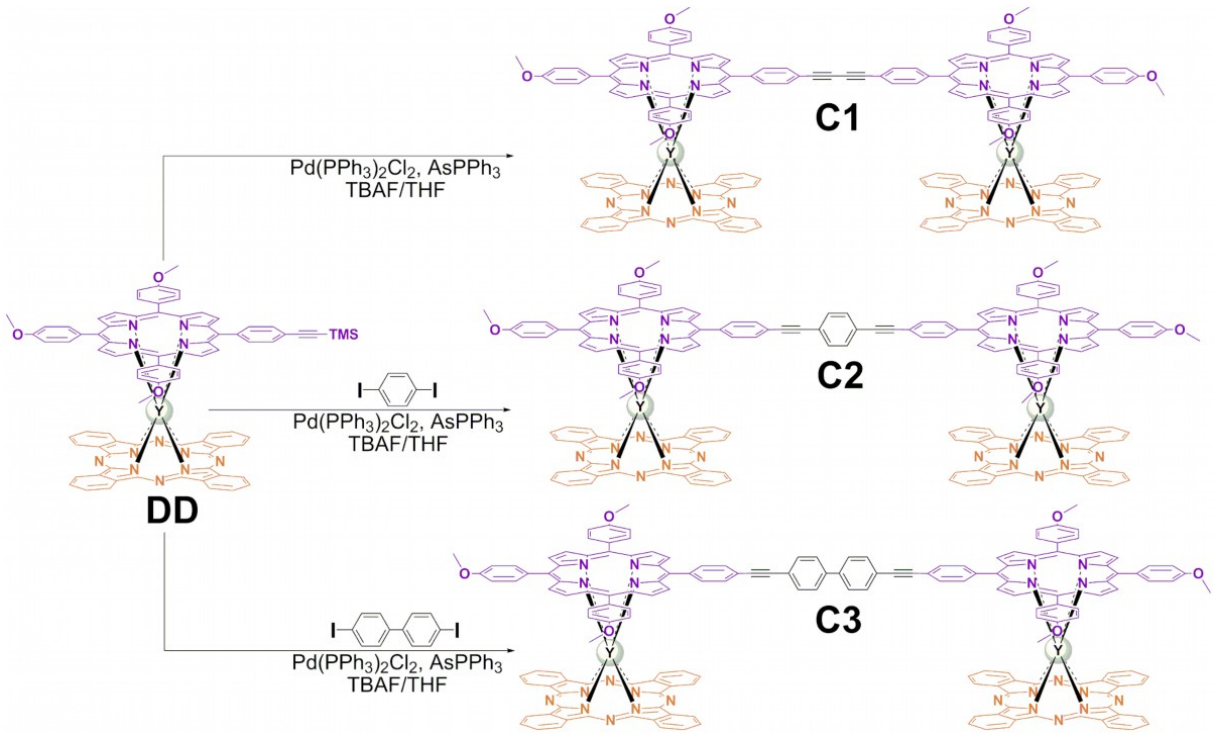

Figure 1: Syntheses and molecular structures of coupled dinuclear sandwich complexes **C1**-**C3**

Due to the presence of $(NBu_4)F$ (henceforth TBAF) in the reaction mixture, the crude product was obtained as an anionic complex. The crude product extracted was subsequently subjected to oxidation by sodium-periodate ($NaIO_4$) followed by column chromatography to obtain the pure product in yields of 6-12%. In order to confirm the structure of the product, from spectroscopic methods, NMR is one of the best options available. However, due to the presence of radical it becomes challenging to analyze the spectra. Hence, in order to remove the radical effect, the ^{1}H-NMR was measured on each sample in 1:1 CD_2Cl_2:DMSO-d_6 solution in the presence of 10% (by volume) hydrazine hydrate, acting as reducing agent. Figure 2 shows a clear difference in the spectra in the δ = 7.75-8.00 ppm region (shaded region), which corresponds to the protons on the linker groups (benzene rings). This confirms the coupling of the monomeric complex with the respective linkers. The identity and purity of the compounds was further corroborated by ESI-MS (Figure S1).

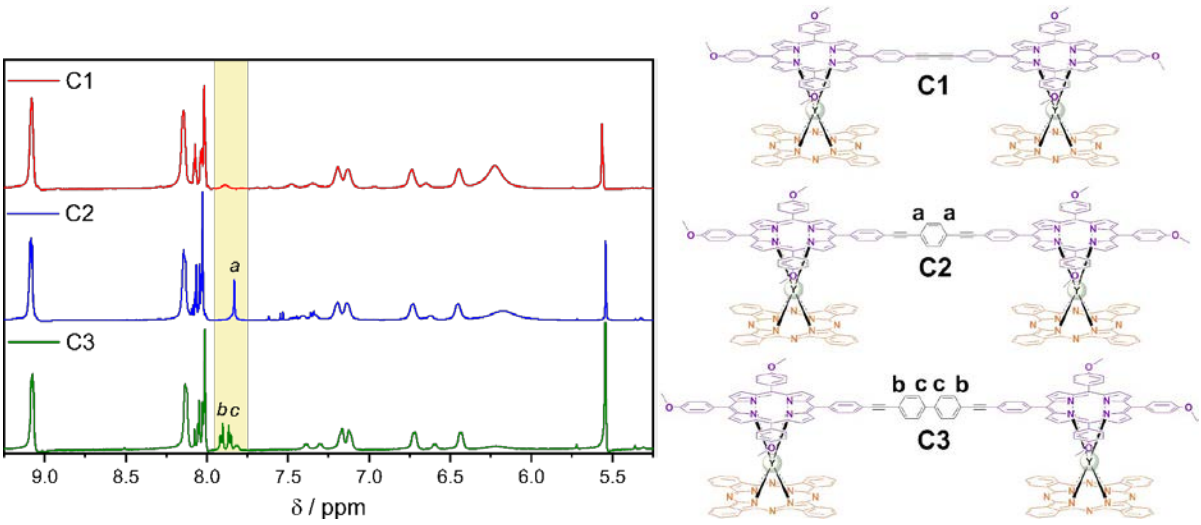

Figure 2: ^{1}H NMR spectra of yttrium analogs of dimeric complexes in CD_2Cl_2-DMSO-d6 (1:1) in the presence of ca. 10% (by volume) hydrazine.

3.2 Solid-state EPR spectroscopy

3.2.1 CW EPR experiments

Preliminary EPR studies of these complexes were carried out using X-band CW EPR to assess the similarities of the mixed-ligand systems with $[Y(pc)_2]^{\cdot}$. These experiments mainly focused on the monomer complex **DD**, while one of the biradical complexes was studied indicatively to fully elucidate this question. **C3** was selected mainly due to the available quantity of the powder sample. Room-temperature solid-state spectra of **DD** and **C3** demonstrated a single Lorentzian resonance, typical of homogeneously broadened spectra (Figures S2, and S3, respectively) similar to that recently obtained for the $[Y(pc)_2]^{\cdot}$ complex.[12]

Variable-temperature CW EPR spectra collected on powders of **DD** and **C3** revealed broad spectra at 4.2 K (FWHM of 0.83 mT and 0.42 mT, respectively). For **DD**, the spectra narrowed continuously upon heating to room temperature (0.24 mT), a behavior consistent with that previously observed for $[Y(pc)_2]^{\cdot}$.[12] For **C3** the narrowing continued up to 50 K reaching 0.29 mT, before demonstrating additional broadening at room-temperature (0.43 mT).

These linewidths, are the combined result both of the spin-spin relaxation time, T_2,[13] as well as exchange-narrowing effects known to affect the spectra of identical spins.[14] These solid-state effects are complicated to fully analyze and beyond of the scope of this work, we therefore limit ourselves to our qualitative discussion.

3.2.2 Pulsed EPR experiments in the solid state

The similarities between **DD** and $[Y(pc)_2]^{\cdot}$, further extended to pulsed EPR in powders. The powered sample of **DD** showed FIDs at room temperature, which were used to record FID-detected nutations (Figure S4), bearing a striking resemblance to the signals previously reported for $[Y(pc)_2]^{\cdot}$.[12] Considering that these studies compellingly demonstrate the similarities between $[Y(pc)_2]^{\cdot}$ and the mixed-ligand systems, no FID-detected pulsed EPR experiments were carried out on **C3**.

3.3 Frozen solution CW EPR spectroscopy

EPR experiments in frozen solutions were carried out in a $CD_2Cl_2/CDCl_3$ 4:1 which showed excellent glassing behavior (Figure S5). Moreover, preliminary studies revealed concentration effects (Figure S6). In particular, 1 m*M* samples were characterized by double resonances with different saturation profiles, which we attributed to aggregation or to intermolecular dipolar interactions. These persisted even after prolonged sonication of the EPR tubes. In turn, dilution to 0.1 m*M* removed these artifacts and further descriptions are given for these samples.

The analysis of CW-EPR experiments in frozen solutions was particularly complicated by the observation of absorption-like spectra at relatively low temperatures and moderate microwave powers (Figures S7). E.g., at a 44 dB attenuation (8.4 μW microwave power) such spectra already appeared at 20 K, whereas no available attenuation could produce derivative-like spectra at 4.2 K. Upon heating, this behavior was mitigated, with regular derivative-like spectra reappearing at temperatures between 35-50 K. At low temperatures, however, this behavior was not mitigated even by testing with different cavities with different power saturation profiles. This is a typical case of passage effects associated with a very slow spin-lattice relaxation,[15,16] as confirmed by pulsed EPR experiments (see below).

This hypothesis was confirmed by comparing ascending vs descending field sweeps, at 40 K, a temperature where these effects are still observed (Figures S8 and S9). These spectra revealed inverted spectra for the ascending vs descending sweeps, which persisted even upon reducing the modulation frequency from 100 to 12.5 kHz. This behavior could be partially mitigated by reducing the scan speed, but it still persisted at 40 K, meaning that very long scans would be required at low temperatures. These experiments were therefore not further pursued.

At these concentrations, any half-field signals due to intra- or intermolecular interactions were masked by $g \sim 4$ impurity signals of our cavities (Figure S10), and were therefore unobservable. We note, however, that this concentration tends to the infinite dilution limit with respect to the intensity of such signals of intermolecular origin.[17]

3.4 Pulsed EPR spectroscopy in frozen solutions

3.4.1 Spin-lattice relaxation studies

The determination of T_1 times was a prerequisite for subsequent pulsed EPR studies. Variable-temperature determinations were carried out indicatively for **DD** (Figure 3) to derive the spin-lattice relaxation law; for the rest of the complexes such determinations were carried out only at the temperature of further experiments. In all cases these were carried out on the maximum absorption as determined by field-sweep echo-detected (FSED) spectra (see below) using saturation recovery experiments. The magnetization traces were fitted to different models, in particular a monoexponential model $M(t) = M_0(1-e^{-(t/T_1)})$ (1), a stretched exponential model $M(t) = M_0(1-e^{-(t/T_1)^{\beta}})$ (2) and a monoexponential law with a spectral diffusion coefficient *q*, $M(t) = M_0(1-e^{-(t/T_1+\sqrt{t/q})})$ (3). These fits confirmed the initial assumption derived from CW spectra: the T_1 times were very long, increasing from 6.9 ms at 95 K to 849 ms at 10 K. Fits to these results (Figure 3) were carried out to a relaxation model comprising Raman and Direct processes:

$$T_1^{-1}(T) = b_R \frac{T}{\Theta_D} J_8\left(\frac{\Theta_D}{T}\right) + b_{Direct} H^{m_{Direct}} T \qquad (4)$$

where the transport integral $J_8\left(\frac{\Theta_D}{T}\right) = \int_0^{\Theta_D/T} \frac{x^8 e^x}{\left(e^x - 1\right)^2} dx$ was calculated numerically.[18]

We should stress that interpretation of spin-lattice relaxation in frozen solutions benefits from models developed for paramagnetic impurities in crystalline matrices. Magnetic molecules in frozen (glassy) solvents may exhibit relaxation pathways due to local vibrational modes.[19] Attempts, however, to include such processes were unsuccessful. Quite large Debye temperatures were derived from these fits, which we attribute to correlations between fitting variables and to the possibility of different processes contributing differently at different temperatures.

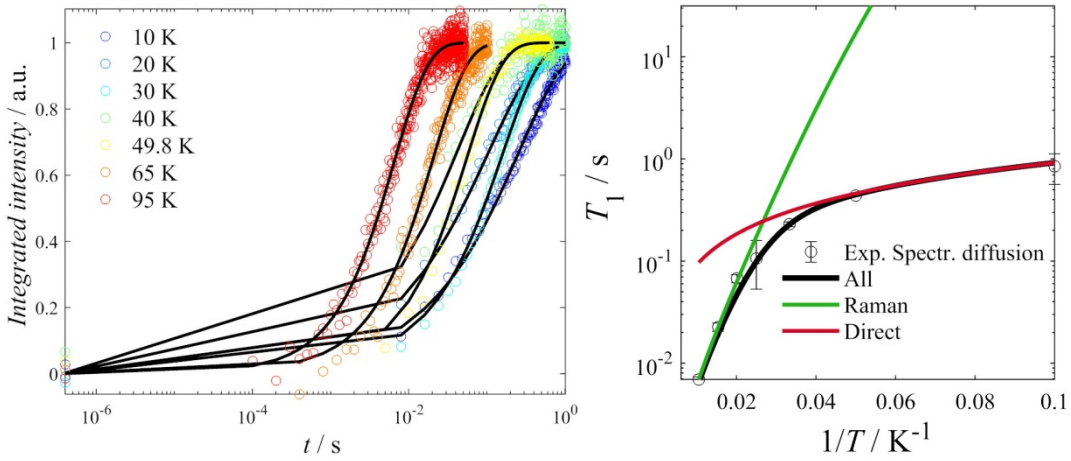

Figure 3. **Left:** Saturation recovery traces for a 0.1 mM CD_2Cl_2:$CDCl_3$ 4:1 frozen solution of **DD** at various temperatures and fits to a monoexponential model comprising spectra diffusion (black lines). **Right:** T_1 times as a function of temperatures and fit to a relaxation model comprising Raman and Direct processes. Best-fit were Θ_D = 244 K, b_{Raman} = 1.0×10^5 s^{-1}, m_{Direct} = 2.0, b_{Direct} = 0.94 s^{-1} $T^{-2.0}$. The vertical error bars indicate the 95% confidence intervals.

At 10 K and below, the T_1 times were too long for the saturation plateau to be attained within the instrumental constrains of our spectrometer, whose PatternJet limited the Shot Repetition Time (SRT) to 2 s, and maximum measurement duration to 1 s.[20] Thus, T_1 times below ~20 K have a considerable degree of uncertainty and the derived values depend on the relaxation model used for the fits. While these limitations can be overcome by using an external trigger, this was not considered as critical in the context of the current work. Further experiments were carried out at higher temperatures where these constrains were overcome.

To ascertain the source of these long relaxation times, we also carried out pulsed EPR experiments on the parent radical complex $[Y(pc)_2]^{\cdot}$ (Figure S11). Interestingly, this also revealed similarly long spin-lattice relaxations, which indicates that the magnetic properties of these mixed-ligand complexes may be related to spin delocalization on the phthalocyanine ring. In particular, since spin-orbit coupling is known to be responsible for mediating the communication of the spin with the lattice vibtrations,[21,19] delocalization on carbon atoms, with their very low spin-orbit coupling, is expected to be a contributing factor to slow spin-lattice

relaxation. Moreover, we carried out such studies on **C3** in an attempt to discern an energy Orbach process with an eventual energy barrier assigned to magnetic interactions (Figure S12). However, no such process was revealed, which we assigned to weak intramolecular interactions.

3.4.2 Field-sweep echo-detected (FSED) spectra

Preliminary FSED spectra were conducted to assess the line shapes and central field values. For **DD**, fits to the 95 and 40 K spectra revealed an almost perfectly Gaussian line shape. Particularly absent from these spectra are any hyperfine features. This is partially explained by DFT calculations which show that most of the spin density is delocalized in C atoms in the phthalocyanines and in the C atoms of the ring of the porphyrin ligand (see section 3.5 and SI). Due to the low natural abundance of magnetic nuclei in carbon we do not expect strong hyperfine couplings which would show up in FSED spectra. As for ^{14}N nuclei, HYSCORE experiments of **C3** showed that such couplings do exist in the "strong" coupling regime ($|A| > 2\omega_{14N}$, where ω_{14N} = 1.07 MHz), but they still are too weak to be resolved by FSED experiments. We tentatively suggest that these weak couplings are due to the low spin densities of the N atoms (see Section 3.5 and SI). The lineshapes can very nicely be reproduced either by isotropic convolutional broadenings, or by anisotropic *H*-strains, that account for unresolved hyperfine couplings.

For comparison, FSED spectra of the parent $[Y(pc)_2]^{\cdot}$ complex were also recorded and showed Gaussian line shapes of very similar widths, also lacking any hyperfine splittings (Figure S13 and Table 1). In addition, FSED spectra collected for **C2** at two different τ delay times demonstrated some modulation-related effects which, nevertheless did not seriously affect the fitted distances (Figure S14).

Table 1. Best-fit parameters to FSED spectra of monomer **DD** and $[Y(pc)_2]^{\cdot}$.

			Isotropic convolutional broadening		Anisotropic broadening
	T (K)	*g*	σ_G (mT_{pp})	σ_L (mT_{pp})	*H* strain *x*/*y*/*z* (MHz)
DD	40	2.0021	0.3455	0.0170	8.8/9.3/11.9
DD	90	2.0022	0.3715	0.0260	7.7/7.9/12.7
$[Y(pc)_2]^{\cdot}$	40	2.0023	0.3210	0.0025	7.6/9.4/10.6
$[Y(pc)_2]^{\cdot}$	90	2.0022	0.3227	0.0024	8.2/8.6/10.6

To extract information on inter-radical distances, the symmetric nature of the biradicals prevented us from carrying out DEER experiments, since we could not apply the requisite pump and probe pulses on separate resonances. We also attempted to carry out RIDME experiments. Although these are better suited for distance measurements of asymmetric "AB" systems (such as metal-radical systems) they have, in some cases, also been successfully used in distance measurements of symmetric biradicals[22,23] and Gd^{III} dimers.[24] Unfortunately, attempts at six-pulse RIDME experiments[25] on **C3** were unsuccessful as no refocused virtual echo could be detected.

Therefore, we instead carried out fits on the FSED spectra, whose shapes should be affected by the anisotropy induced by dipole-dipole interactions. For these fits, the fitted linewidth values of the mononuclear spectrum were used as fixed variables. Moreover, it was considered that no

intermolecular dipolar interactions were operative. Indeed, a Poisson distribution predicts that the vast majority (99.6%) of intermolecular distances at this concentration is above 25 Å (Figure S15).

The first limitation of this approach is that its applicability starts decreasing for distances above ~25 Å, as the line shape of the dipole-coupled dimer starts approaching that of the monomer. E.g., for absorption-type signals with Gaussian peaks of 0.36 mT_{pp} (peak-to-peak) linewidths, the two peaks coalesce into a single one approximately at 16 Å. The effective linewidth of the biradical system decreases and reaches 0.37 mT_{pp} for distances of 30 Å. These are illustrated in Figure 4 and can be compared to the various interspin distances shown in Table 2.

The above means that while we may be able to determine distances between spin densities residing on the proximal atoms of the spin systems, dipole interactions between distal atoms would not yield anisotropies strong enough to be detected by their influence on the EPR line shapes. These distances are shown in Table 2 and for **C1-*trans*** in the bottom of Figure 4. With the longer biradicals exhibiting a main peak of effective linewidths of ca. 0.45 mT_{pp}, this approach was applicable for at least a significant part of the spin densities.

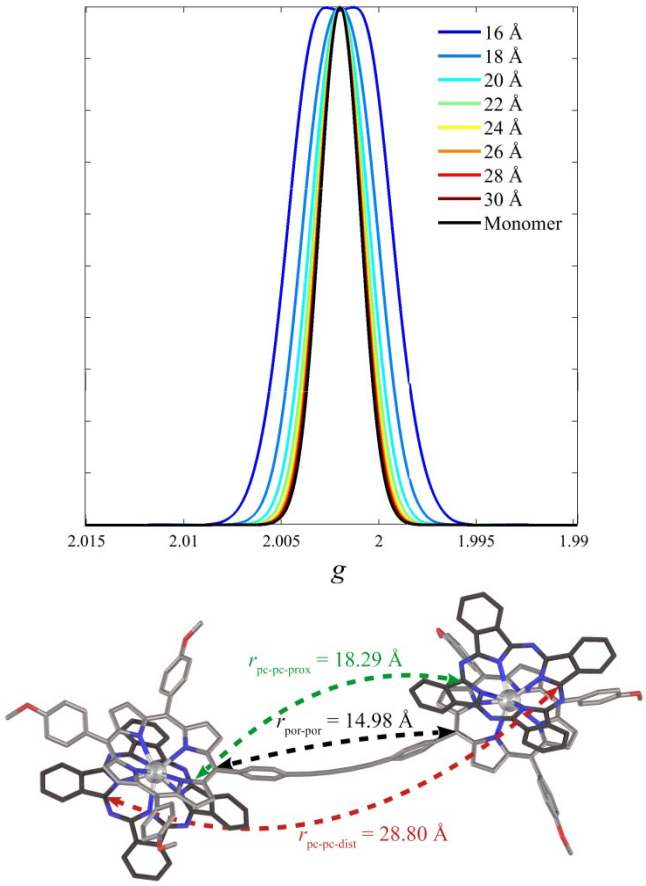

Figure 4. **Top:** Line shapes of simulated FSED spectra of symmetric dipole-dipole coupled species. **Bottom:** Distances between different atoms of the delocalized system **C1-*trans***, derived from a calculated structure.

Table 2. Calculated interatomic distances for the *trans* conformations of **C1**-**C3**. Distance $r_{\text{por-por}}$ refers to the porphyrin carbon atoms on which the tether is grafted.

Conformation	$r_{\text{por-por}}$ (Å)	$r_{\text{pc-pc-prox}}$ (Å)	$r_{\text{pc-pc-dist}}$ (Å)
C1-*trans*	14.98	18.29	28.80
C2-*trans*	19.26	22.20	34.30
C3-*trans*	23.62	26.20	38.54

A second limitation concerns the hypothesis that spin densities reside solely on the pc/por systems. Indeed, theoretical calculations on long-chain bridged biradicals have shown this not always to be the case,[26–28] with a "spin leakage" occurring, much more so over conjugated organic tethers than aliphatic ones, in some cases leading to magnetic exchange.

This raises the point of the treatment of eventual superexchange terms. In subsequent analysis superexchange terms ($\hat{H}_{\text{exch}} = J_{ij}\hat{\mathbf{S}}_i\hat{\mathbf{S}}_j$) are not considered for any of the biradicals, for two main reasons.

The first concerns experimental complications arising in their determination by other methods. E.g., due to the expected low values of such couplings, SQUID magnetometry in the solid state might reasonably be dominated by intermolecular interactions which can often be quite significant.[29–31] This would require SQUID experiments in solution to unequivocally determine *J*, in which precise diamagnetic corrections are quite complicated to derive. Alternately, variable-temperature studies of the intensities of half-field signals might be employed, which are also quite demanding and entail significant uncertainties.

The second reason is the lack of relevance of such interactions in the current context. Indeed, these are not expected to be discernible in the field-swept EPR spectra of symmetric biradicals ($\mathbf{g}_1 = \mathbf{g}_2$), experiencing no hyperfine splittings. Hyperfine-split spectra of asymmetric biradicals are influenced by, and can yield information on, the ratio of J/A,[32] however this is not the case for the systems studied herein. Therefore, in the scope of this work we have disregarded superexchange couplings, if any are operative.

Preliminary fits were carried out to a point-dipole model previously described.[33] This model yielded relatively coherent results for **C2** and **C3** as shown in Figure 5, with the main spectral feature being well reproduced by distances reasonably close to the por-por ones. However, the presence of satellite features prompted us to introduce minor components of smaller interspin distances, a modification constituting an approximation to the distributed-dipole model.[34] These features can be rationalized by considering the presence of spin density over the organic tether. This "leaky tether" hypothesis was further tested by DFT calculations (*vide infra*). It is noteworthy that the satellite features at 40 K were quite weak, making their inclusion in the fits less reliable. These are subsequently not shown. However, these were more pronounced at 95 K allowing us to meaningfully fit their relative intensities.

The above results are summarized in Figure 5 and Table 3.

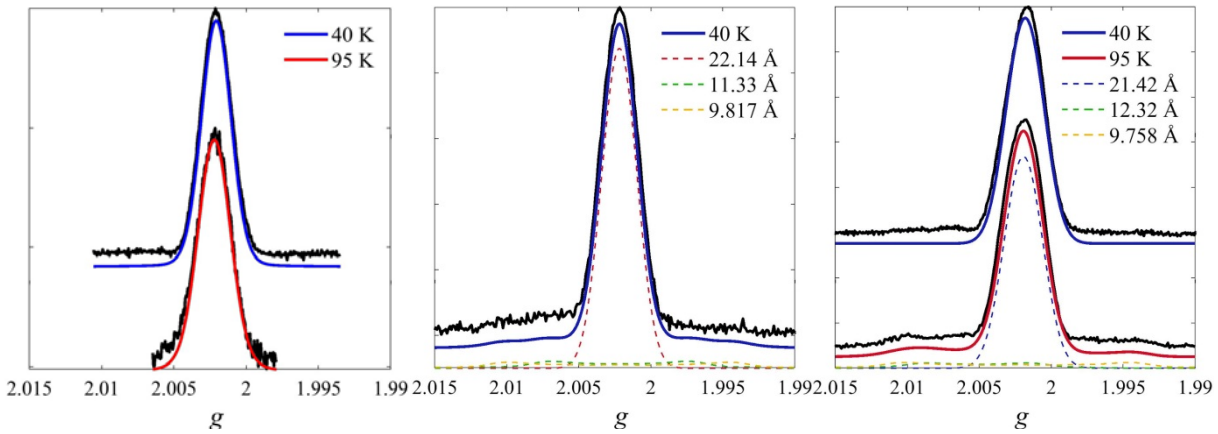

Figure 5. **Left.** FSED spectrum for a 0.1 mM CD_2Cl_2:$CDCl_3$ 4:1 frozen solution of **DD** and fit to a single resonance, with best-fit parameters shown in Table 1. The linewidths of these spectra were then used as a fixed variables to fit the spectra of dimers. **Middle.** FSED spectrum for a 0.1 mM CD_2Cl_2:$CDCl_3$ 4:1 frozen solution of **C2** at 40 K and fit to two subcomponents. **Right.** Fit to FSED spectra of **C3**. The 40 K spectrum was fitted to only one dipole-dipole distance. The 95 K spectrum was fitted to three subcomponents. Best-fit parameters for the spectra of **C2** and **C3** are shown in Table 3. Experimental conditions:. f_{MW} = 9.81456 GHz (**DD**, 40 K), 9.7575 GHz (**DD**, 95 K), 9.75515 GHz (**C2**), 9.81331 GHz (**C3**, 40 K), 9.75577 GHz (**C3**, 95 K); τ = 1170 ns (**DD**, **C1**), 1150 ns (**C2**, **C3**), $\pi/2$ = 16 ns, 150 ns integrator gate.

Table 3. Best-fit parameters from fits of the FSED spectra of **C2** and **C3** to a set of point-dipole pairs. In each case, the relative weight of the central resonance is defined as w = 1

Complex	$r_{central}$ (Å)	r_1 (Å), w_1	r_2 (Å), w_1
C2 (40 K, τ = 356 ns)	21.2 (w = 1)	12.1 (w_1 = 0.23)	9.78 (w_2 = 0.039)
C2 (40 K, τ = 1150 ns)	22.1 (w = 1)	11.3 (w_1 = 0.087)	9.81 (w_2 = 0.10)
C3 (40 K)	21.3 (w = 1)	-	-
C3 (95 K)	21.4 (w = 1)	12.3 (w_1 = 0.079)	9.75 (w_2 = 0.13)

On the other hand, in the case of the shortest dimer, **C1**, the line shape of the FSED spectrum was deformed due to modulations of the echo shape when the magnetic field departed from a narrow region (~0.1 mT) off the main resonance (Figure 6). In particular, close to the main peak, the real part of the echo presented the expected form, whereas off the maximum resonance it exhibited strong modulations. This hampered the correct signal integration, consequently, the FSED spectrum could not be reliably fitted. Nevertheless, the off-peak echo was used to draw conclusions about the spin state at that field (see Spin nutation experiments).

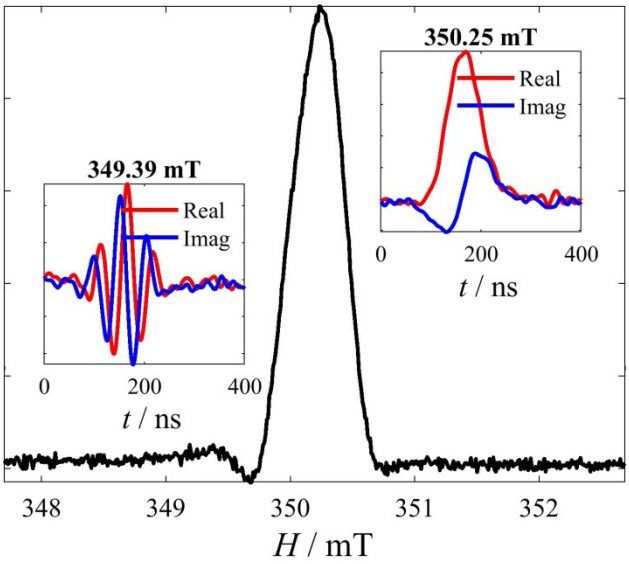

Figure 6. FSED spectrum for a 0.1 mM CD_2Cl_2:$CDCl_3$ 4:1 frozen solution of **C1** at 40 K (τ = 1.19 μs, f = 9.81315 GHz, $\pi/2$ = 16 ns, 150 ns integrator gate). The insets show indicative Hahn echo traces at two magnetic fields near and further away from the maximum.

It is noteworthy that these echo modulations are reminiscent of similar signals detected for a benzene solvate of the α,γ-bisdiphenylene-β-phenylallyl (BDPA) radical,[35] attributed at that particular case to strong spin-photon coupling with the cavity and to the excitation of polariton modes. Despite this similarities, however, in that work the sample was a 21.5 mg pure BDPA pellet, containing ca. 1.2×10^{19} spins, studied at 7 K in a custom-built Fabry–Pérot resonator. In our case, the sample is a 0.1 mM solution containing ca. 6×10^{15} biradicals, studied at 40 K in a standard Bruker dielectric resonator. Overall, that sample was 10^4 times larger than ours and also studied at lower temperatures in a resonator specifically designed to achieve very strong spin-photon couplings.

During the review process it was suggested that this is a manifestation of passage through a relatively sharp signal using narrow pulses, with one of the reviewers supplying similar echoes from γ-irradiated silica. Indeed, such signals have also been observed in regular resonators,[36] or during electrically-detected magnetic resonance experiments.[37] They can be rationalized by the consideration of an echo as two back-to-back FIDs evolving forward and backward in time;[38] when off-resonance, these FIDs will exhibit an oscillatory behavior.

Actually, a method has been proposed for the analysis of echoes to achieve better sensitivities and resolutions with respect to FSED spectra collected by echo integration.[36] Based on that method we carried out complex FFT analysis on the real and imaginary parts of the echoes and found that they are characterized by negative and positive frequency offsets for $B_0 < B_{res}$ and $B_0 > B_{res}$, respectively. The offset was a linear function of the applied magnetic field, with a rate of ~1.8 MHz G^{-1} (Figure 7). These results highlight the often overlooked importance of the direct dimension in pulse EPR spectroscopy.[39]

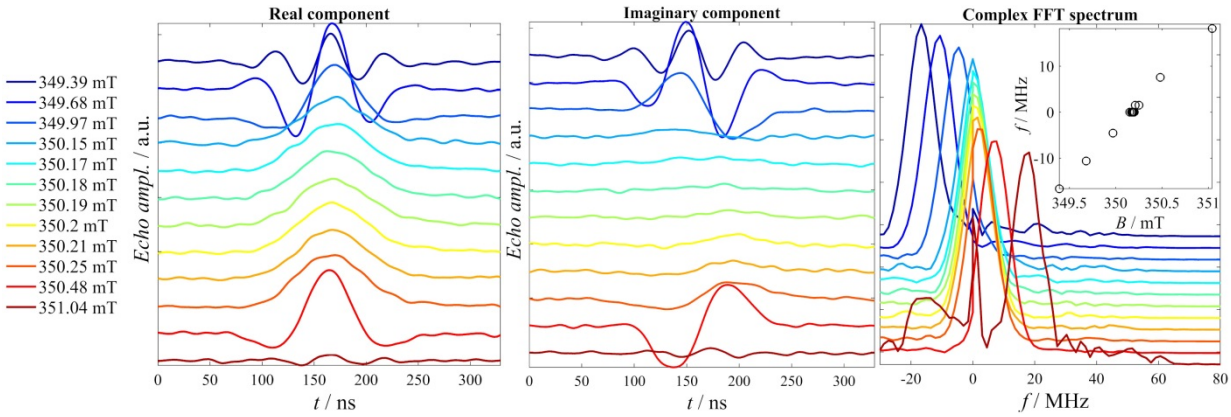

Figure 7. Real (left) and imaginary (center) components of Hahn echoes for a 0.1 mM CD_2Cl_2:$CDCl_3$ 4:1 frozen solution of **C1** (T = 40 K, τ = 1.19 μs, f = 9.81315 GHz) as a function of the magnetic field. The FFT on the complex signal (right) shows frequency offset as a function of the magnetic field (shown in the plot inset).

3.4.3 Echo-decay experiments

Hahn-echo decay experiments were carried out to assess the phase-memory times, T_m, of the various samples. These were carried out at the magnetic field corresponding to each FSED spectrum's maximum, and at a 40 K temperature, at which the T_1 times were short enough to allow a $5T_1$ SRT at a reasonable experimental duration, and the T_m long-enough to observe sufficiently strong echoes.

The presence of very deep modulations (Figure S16) significantly hampered the quantitative treatment of the echo-decay traces. Attempts to decrease the modulation depth by softer and more selective pulses required 256/512 ns pulses to substantially decrease most of the modulations, though the initial one around 1 μs persisted (Figure S17). We tentatively attribute this modulation to couplings to ^{14}N nuclei established by HYSCORE experiments. Fits to the latter part of the echo decay trace, which was free of modulations, yielded T_M times between 5 and 9 μs (see Supporting Information). It is noteworthy that these results were close matched by echo-decay studies on solution samples of the parent $[Y(pc)_2]^{\cdot}$ complex.

It should be noted that spin diffusion involving ^{1}H nuclei could participate in the shortening of the coherence time of these radicals. Indeed, while the experiments were carried out in deuterated solvents, the ^{1}H nuclei of the undeuterated phtalocyanine/porphyrin ligands, gives an effective ^{1}H concentration of 4 mM for the monoradicals and 8 mM for the biradicals, which are quite significant. Actually, the larger ^{1}H concentration of the biradicals is also reflected in their T_M times, which are approximately half those of monoradicals species. Deuteration of the ligands would be a potential avenue to further increase the coherence time of these systems.

Another factor that may be considered for the shortening of coherence times are molecular motions which can occur even in frozen solvents at low temperatures. Given the quasicylindrical shape of the monoradicals, they may undergo librational motions around their central axis, thereby introducing an additional decoherence pathway. It might therefore be expected that the less symmetric, hence more constrained, biradicals move less freely in the glassy matrix.

If such is the case, then the biradicals constitute a case where one factor that accelerates decoherence, i.e. large ^{1}H concentration, coexists with a factor that decelerates it, i.e. diminished mobility. It stems therefore that increase of coherence times could be achieved by targeting

molecular shapes with small mobility and high rigidity, e.g. by long and rigid side-groups, while taking care to keep the ^{1}H count low.

3.4.4 Spin nutation experiments

Spin nutation experiments were carried out to assess the ability to coherently drive the spin of the compounds at 40 K. Moreover, these experiments allow us to unequivocally establish the spin multiplet character within which each transition takes place, since the nutation frequency of a transition between states M_S and M_S +1 within a multiplet S is given by:[40]

$$f_{nut} = \frac{\mu_B g B_1}{\hbar}\sqrt{S(S+1) - M_S(M_S+1)} \qquad (7)$$

Initial experiments were carried out at the central resonance with variable MW powers, with the nutation traces of **DD** (Figure 8) and $[Y(pc)_2]^{\cdot}$ (Figure S19) being used as calibration standards for the $|S_T, M_S\rangle = |1/2, \pm 1/2\rangle$ transitions. All experiments revealed oscillations, identified to be Rabi oscillations by the linear dependence of their frequency on B_1 (Figures S18 and S19). Comparison of the frequencies between all complexes confirmed that the nature of the central transition is $|1/2, \pm 1/2\rangle$, while fitting parameters to an exponentially damped oscillation gave comparable results (Table 4). At higher powers we observe a decrease of τ_R, which we assign to "driven decoherence",[41] but also an overall decrease of the signal intensity, which we assign to larger turning angles at higher powers, requiring longer SRT than the ones used at lower MW power experiments.[42]

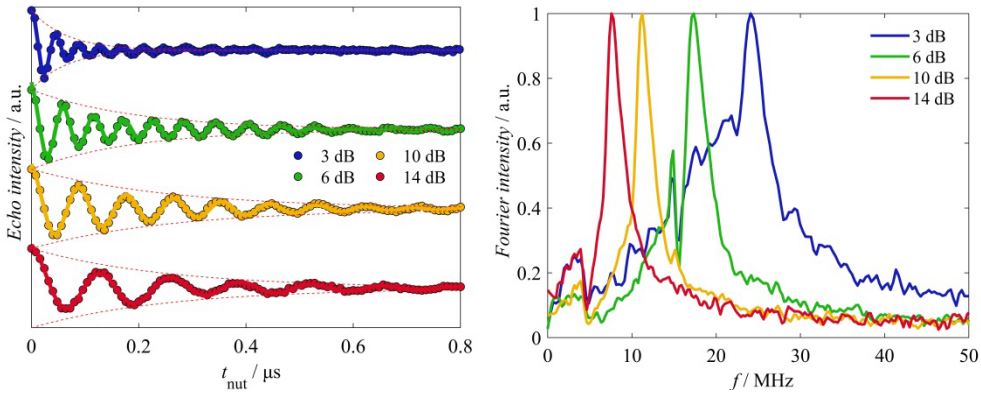

Figure 8. **Left:** Spin nutation for a 0.1 mM CD_2Cl_2:$CDCl_3$ 4:1 frozen solution of **DD** at various microwave powers at 40 K. **Right:** Fourier transform spectra of the nutation traces.

However, the particular behavior of **C1** prompted us to further assess the satellite resonance. Due to the modulated echo (Figure 6, left inset and Figure 7) a narrow integration window was selected for the detection of the nutation traces. Nutation experiments at this field also yielded oscillations with a frequency dependent on the MW power (Figure S20), thus also confirming these to be Rabi oscillations. Nevertheless, at the same attenuation level (6 dB) the nutation frequency at that field was 23.8 MHz, i.e., higher by a factor of 1.42 ~ √2 than the respective frequency (16.8 MHz) at the center of the resonance and at the same attenuation (Figure 9). Based on Eq. 7, this indicates that this resonance stems from a $M_S = -1$ to $M_S = 0$ transition within a $S = 1$ spin multiplet.

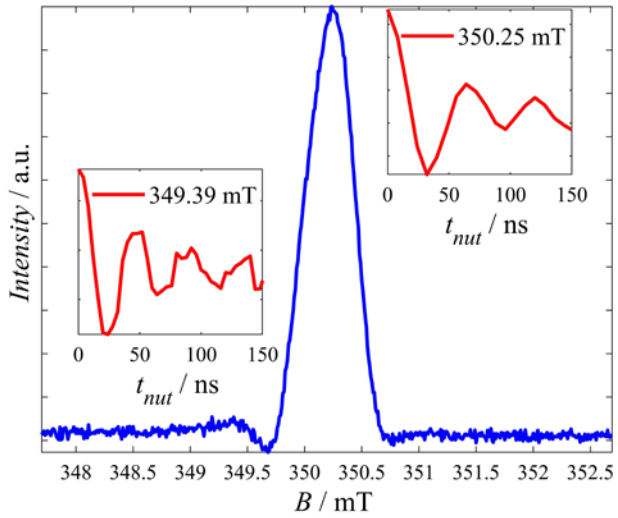

Figure 9. FSED spectrum for a 0.1 mM CD_2Cl_2:$CDCl_3$ 4:1 frozen solution of **C1** with the Rabi oscillations at the different magnetic fields as insets.

This behavior is reminiscent of that previously observed in a Cu^{II}-nitroxyl radical complex whose spectrum was interpreted in the framework of an exchange-coupled "AB" system. In that system, the appearance of the FSED spectrum depended on the MW power of the pulses, as the external vs internal parts of the spectrum corresponded to different effective *S* values and, therefore, turning angles for the same MW power.[43] In our case, the two $S = 1/2$ spins are identical, yet they also give rise to transitions corresponding to different effective spin states.

An additional interpretation was considered for this variance in nutation frequencies, in particular that it is characteristic of an off-resonance FID. Although the signal was indeed from an off-resonant FID, the nutation frequency itself is qualitatively distinct, as it corresponds to the variation of the echo integral as a function of the nutation pulse length. Indeed, the nutation frequency depends on the MW power (see Fig. S20) demonstrating that it is a Rabi oscillation.

Table 4. Dependence of the Rabi damping times on the MW power attenuation

Complex	τ_R (μs)			
	3 dB	**6 dB**	**10 dB**	**14 dB**
DD	0.065(8)	0.19(1)	0.26(2)	0.25(1)
C1	0.087(5)	0.073(6)	0.13(1)	0.14(2)
C2	0.093(14)	0.10(1)	0.13(1)	0.13(2)
C3	0.083(6)	0.14(1)	0.17(1)	0.18(1)

The numbers in parentheses are the 95% confidence interval.

3.5 Theoretical studies

To get a better understanding of the FSED spectra, we performed *ab initio* calculations based on density functional theory (DFT) on all the molecules using the quantum package CP2K.[44] In addition to the *cis* structures we also optimized and simulated the "*trans*" geometries. The *trans*

structures were those in which one of the two [Y(pc)(por)] molecules was rotated 180° around the organic tethers (see methods' section for details). The stability of each of the *cis* structures was analyzed in terms of its DFT energy by comparing it to the corresponding *trans* geometry. The results are displayed in Table 5.

Table 5. Relative energies of the three simulated compounds. The energy differences clearly show that the *trans* arrangement is more stable than the *cis* one. All the simulations were carried with identical precision and DFT parameters.

System	$\Delta E_{cis\text{-}trans}$ (eV)
C1	0.257
C2	0.222
C3	0.152

In general, not only are the *trans* configurations more stable, but the organic linker adopts a straight geometry, in contrast to a more curved one of the *cis* ones. Moreover, the chain length influences the relative stability of the two conformations, with the shortest chains imposing a greater energetic preference to the *trans* conformation.

Since the spin localization in similar systems is closely related to phenomena such as magnetic coupling or electronic transport, we also analyzed the spin fingerprints on each of the systems. In contrast to simple double-decker compounds, the spin density is spread across all the carbon atoms of the phthalocyanine ligands as well as in the carbon atoms of the ring in the porphyrin. A substantial difference between the **C1-*cis*** and **C1-*trans*** is that a larger spin density leakage is observed into the linker in **C1-*trans***, as can be observed in Figure 10b. This behavior seems to diminish as the distance between both double-decker complexes increases (see Figure S21). This observation is in line with that calculated for similar supramolecular multiradical systems.[27,28]

The above findings are in line with the calculations of the singly-occupied molecular orbitals (SOMO) for each spin. These suggest that in the *trans* conformation of **C1** the SOMOs are more extended over to the neighboring double-decker system (Figures S22 vs S23, top). These results are coherent with spin nutation experiments demonstrating the presence of different spin states off the main resonance, presumably due to stronger coupled densities on linker atoms.

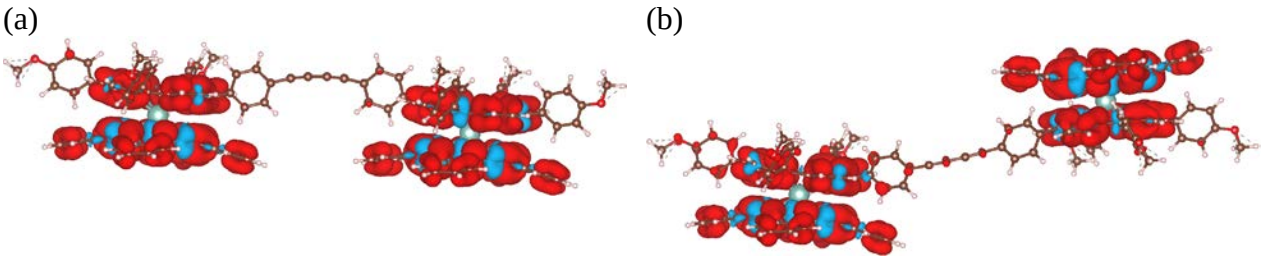

Figure 10: Spin density of **C1-*cis*** and **C1-*trans*** in a) in b) respectively. Red/blue correspond to α/β spins, respectively. It can be seen that in **C1-*cis***, most of the density is delocalized over the carbon atoms in both of the ligands. Nevertheless, **C1-*trans*** presents spin leakage into some of the carbons in the organic tethers.

To further corroborate the above, and also to rationalize the lack of hyperfine couplings in the EPR spectra of these complexes, we performed Hirshfeld analysis to derive the atoms

contributing to its total spin magnetization. Indicatively, we selected the two conformations of **C1** (Tables S2-S5 and Figures S24, S25). These calculations show that the α-spin density preponderantly resides on C atoms and the β-spin density preponderantly so on N atoms. Moreover, the α-spin density is roughly 8.5 and 8 times greater than the β-spin density, for the *cis* and *trans* conformations, respectively, thus explaining the lack of hyperfine signals in EPR spectra.

Moreover, we correlate these results with preliminary HYSCORE studies carried out indicatively on **C3** at 95 K (Figure S26). These reveal signals in the (-,+) quadrant clearly demonstrating hyperfine couplings with ^{14}N falling within the "strong" coupling regime ($|A| > 2\omega_{14N}$, where ω_{14N} = 1.07 MHz). Indeed, simulations indicate values A_{xy} = -5.61 MHZ, A_z = -3.78 MHz, Q_x = -0.08 MHz, Q_y = -1.52 MHz, Q_z = 1.60 MHz. These couplings, remain quite weak to be adequately resolved in FSED experiments. We tentatively assign their weak intensity to the low spin density residing on N atoms.

4 Discussion

In this work we have proposed a new strategy to design and synthesize stable bis-"double decker" systems, using molecular engineering principles to carefully control their distances and, hence, their magnetic interactions. To do this we used mixed-ligand pc/por double-decker moieties, taking advantage of the synthetic versatility offered by the *meso*-positions of the por ligands. To the best of our knowledge this is the first such approach to tackle this problem in a rationally designed manner.

Another objective of this work was to compare the magnetic properties of the "parent" $[Y(pc)_2]^{\cdot}$ radical system with the those of the mixed-ligand $[Y(pc)(por)]^{\cdot}$ analogues. Experiments both in the solid state and in solution clearly demonstrated close similarity of these magnetic properties. Indeed, the **DD** monomer perfectly reproduces the behavior of $[Y(pc)_2]^{\cdot}$, in both powders and frozen solutions and for several different experiments.

This work has also demonstrated the synthetic feasibility to use the $[Ln(pc)_2]^{\cdot}$ platform to engineer larger spin systems with predefined architectures and custom-designed magnetic interactions. EPR studies and DFT calculations showed that the rigid supramolecular tether is not an innocent component of the system, as it can become "leaky" due to spin delocalization below a certain length and/or at specific conformations. In that case, significant spin density can leak onto its atoms, introducing new components to the magnetic behavior of the dimers.

Interestingly, we note that studies such as this, entailing: (i) series of carefully engineering biradical systems, studied in detail by a combination of (ii) advanced EPR and (iii) theoretical methods, are quite uncommon. Numerous past studies often focus on one of those aspects or on single biradicals. This combined approach is very rare, and has allowed us to bring forth finer, and previously unobserved, details of the magnetic structures of these systems. These are particularly relevant in regard to surface deposition of such molecules for the construction of molecular devices, a domain in which the $[Ln(pc)]^{\cdot}$ platform has been shown to be particularly adapted.[45] The details of the molecular conformation of such surface-deposited molecules would be a critical parameter in their utility as device components.

A salient point in this respect is the observation made by nutation experiments that resonances away from the main peak can be attributed to S = 1 spin systems, at least in the case of the

shortest tethers. This may suggest that the spin leakage and the significantly shortest interspin distances to which it gives rise, create a system with a different spin character.

During these studies, it was also revealed that radical complexes based on the [Y(pc)]˙ moiety exhibit quite long spin-lattice relaxation times in frozen solution. This observation, along with the possibility to design asymmetric biradicals, offers some intriguing perspectives, especially relating to the use of such systems in DNP, where long T_1 times are a particular advantage. In addition, it has been proposed that biradicals with two distinct electronic Larmor frequencies, whose difference is equal to the Larmor frequency of the nucleus under rf excitation should maximize the DNP enhancement.[46]

On a parallel track, such asymmetric biradical systems might constitute ideal platforms to implement molecular CNOT gates, whereby the two qubits are weakly coupled due to dipolar interactions, while their different *g*-values might allow the individual addressing by different microwave frequencies. Recent developments in the design of pulsed EPR experiments render this perspective quite intriguing.[47]

Overall, we have successfully implemented molecular engineering principles to construct biradicals with designed interspin distances, and we have demonstrated their dipole-dipole interactions. Pulsed EPR experiments and DFT calculations showed that while spin delocalization over the rigid organic tether could not be entirely prevented, this "spin leakage" could be minimized by lengthening of the tether. Indeed, fits to a version of a distributed-dipole model showed that roughly 75-80% of the spin densities of the longer-chained biradicals **C2** and **C3** were based on the pc/por ring systems.

In light of the previously mentioned perspectives of biradical use as DNP polarizing agents and/or CNOT gate elements, we are currently looking into the preparation of asymmetric biradical systems, based on the [Y(pc)]˙ platform.

5 Acknowledgments

Financial support from the CNRS research infrastructure INFRANALYTICS (FR2054) for conducting the research is gratefully acknowledged. AKB thanks the Baden-Württemberg Stiftung for financial support through the MOLTRIQUSENS project. EMP thanks the Panamanian National System of Investigators (SNI, SENACYT) for support. JEOP thanks DFG grants FE 1776/2-1 and WE 1863/34-1. We thank Prof. Joris van Slageren and Dr. David Hunger (University of Stuttgart), for helpful discussions.

6 Supporting Information

PDF file with supporting information contains: (i) synthetic procedures and characterization, (ii) materials and methods for physical studies and theoretical calculations, (iii) additional CW and pulse EPR experiments on powders and frozen solutions, (iv) additional results of theoretical calculations and spin density analysis.

7 References

(1) Vincent, R.; Klyatskaya, S.; Ruben, M.; Wernsdorfer, W.; Balestro, F. Electronic Read-out of a Single Nuclear Spin Using a Molecular Spin Transistor. *Nature* **2012**, *488* (7411), 357–360. https://doi.org/10.1038/nature11341.

(2) Godfrin, C.; Ferhat, A.; Ballou, R.; Klyatskaya, S.; Ruben, M.; Wernsdorfer, W.; Balestro, F. Operating Quantum States in Single Magnetic Molecules: Implementation of Grover's Quantum Algorithm. *Physical Review Letters* **2017**, *119* (18), 187702. https://doi.org/10.1103/PhysRevLett.119.187702.
(3) Ishikawa, N.; Iino, T.; Kaizu, Y. Interaction between F-Electronic Systems in Dinuclear Lanthanide Complexes with Phthalocyanines. *J. Am. Chem. Soc.* **2002**, *124* (38), 11440–11447. https://doi.org/10.1021/ja027119n.
(4) Horii, Y.; Katoh, K.; Yasuda, N.; Breedlove, B. K.; Yamashita, M. Effects of f–f Interactions on the Single-Molecule Magnet Properties of Terbium(III)–Phthalocyaninato Quintuple-Decker Complexes. *Inorg. Chem.* **2015**, *54* (7), 3297–3305. https://doi.org/10.1021/ic502951t.
(5) Katoh, K.; Isshiki, H.; Komeda, T.; Yamashita, M. Multiple-Decker Phthalocyaninato Tb(III) Single-Molecule Magnets and Y(III) Complexes for next Generation Devices. *Coordination Chemistry Reviews* **2011**, *255* (17–18), 2124–2148. https://doi.org/10.1016/j.ccr.2011.02.024.
(6) Moreno-Pineda, E.; Klyatskaya, S.; Du, P.; Damjanović, M.; Taran, G.; Wernsdorfer, W.; Ruben, M. Observation of Cooperative Electronic Quantum Tunneling: Increasing Accessible Nuclear States in a Molecular Qudit. *Inorg. Chem.* **2018**, *57* (16), 9873–9879. https://doi.org/10.1021/acs.inorgchem.8b00823.
(7) Katoh, K.; Yasuda, N.; Damjanović, M.; Wernsdorfer, W.; Breedlove, B. K.; Yamashita, M. Manipulation of the Coordination Geometry along the C_4 Rotation Axis in a Dinuclear Tb^{3+} Triple-Decker Complex via a Supramolecular Approach. *Chem. Eur. J.* **2020**, *26* (21), 4805–4815. https://doi.org/10.1002/chem.201905400.
(8) Katoh, K.; Horii, Y.; Yasuda, N.; Wernsdorfer, W.; Toriumi, K.; Breedlove, B. K.; Yamashita, M. Multiple-Decker Phthalocyaninato Dinuclear Lanthanoid(Iii) Single-Molecule Magnets with Dual-Magnetic Relaxation Processes. *Dalton Trans.* **2012**, *41* (44), 13582. https://doi.org/10.1039/c2dt31400b.
(9) Morita, T.; Damjanović, M.; Katoh, K.; Kitagawa, Y.; Yasuda, N.; Lan, Y.; Wernsdorfer, W.; Breedlove, B. K.; Enders, M.; Yamashita, M. Comparison of the Magnetic Anisotropy and Spin Relaxation Phenomenon of Dinuclear Terbium(III) Phthalocyaninato Single-Molecule Magnets Using the Geometric Spin Arrangement. *J. Am. Chem. Soc.* **2018**, *140* (8), 2995–3007. https://doi.org/10.1021/jacs.7b12667.
(10) Wang, R.; Li, R.; Li, Y.; Zhang, X.; Zhu, P.; Lo, P.-C.; Ng, D. K. P.; Pan, N.; Ma, C.; Kobayashi, N.; Jiang, J. Controlling the Nature of Mixed (Phthalocyaninato)(Porphyrinato) Rare-Earth(III) Double-Decker Complexes: The Effects of Nonperipheral Alkoxy Substitution of the Phthalocyanine Ligand. *Chem. Eur. J.* **2006**, *12* (5), 1475–1485. https://doi.org/10.1002/chem.200500733.
(11) Wang, H.; Wang, K.; Tao, J.; Jiang, J. Twist Angle Perturbation on Mixed (Phthalocyaninato)(Porphyrinato) Dysprosium(Iii) Double-Decker SMMs. *Chem. Commun.* **2012**, *48* (24), 2973. https://doi.org/10.1039/c2cc16543k.
(12) Boudalis, A. K.; Olivares-Peña, J.-E.; Moreno-Pineda, E.; Fediai, A.; Wenzel, W.; Turek, P.; Ruben, M. Room-Temperature Spin Nutations in a Magnetically Condensed Phase of $[Y(Pc)_2]^{\cdot}$. *Chem. Commun.* **2021**, 11505-11508 10.1039.D1CC05491K. https://doi.org/10.1039/D1CC05491K.
(13) Weil, J. A.; Bolton, J. R. *Electron Paramagnetic Resonance: Elementary Theory and Practical Applications*, 2nd ed.; Wiley-Interscience: Hoboken, N.J, 2007, chapter 10.

(14) Abragam, A.; Bleaney, B. *Electron Paramagnetic Resonance of Transition Ions*; Oxford classic texts in the physical sciences; Oxford University Press: Oxford, 2012, pp. 58 & 527-529.
(15) Weger, M. Passage Effects in Paramagnetic Resonance Experiments. *Bell System Technical Journal* **1960**, *39* (4), 1013–1112. https://doi.org/10.1002/j.1538-7305.1960.tb03951.x.
(16) Eaton, S. S.; Eaton, G. R. Electron Paramagnetic Resonance. In *Ewing's analytical instrumentation handbook*; Cazes, J., Ewing, G. W., Eds.; Marcel Dekker: New York, 2005; pp 349–398.
(17) Eaton, S. S.; More, K. M.; Sawant, B. M.; Eaton, G. R. Use of the ESR Half-Field Transition to Determine the Interspin Distance and the Orientation of the Interspin Vector in Systems with Two Unpaired Electrons. *J. Am. Chem. Soc.* **1983**, *105* (22), 6560–6567. https://doi.org/10.1021/ja00360a005.
(18) Pearson, T. J.; Laorenza, D. W.; Krzyaniak, M. D.; Wasielewski, M. R.; Freedman, D. E. Octacyanometallate Qubit Candidates. *Dalton Trans.* **2018**, *47* (34), 11744–11748. https://doi.org/10.1039/C8DT02312C.
(19) Eaton, S. S.; Eaton, G. R. Relaxation Times of Organic Radicals and Transition Metal Ions. In *Distance Measurements in Biological Systems by EPR*; Berliner, L. J., Eaton, G. R., Eaton, S. S., Eds.; Biological Magnetic Resonance; Springer US: Boston, MA, 2000; pp 29–154. https://doi.org/10.1007/0-306-47109-4_2.
(20) Weber, R. T. *ELEXSYS E 580 USER'S MANUAL, v. 2.0*; Bruker BioSpin Corporation: Billerica, MA USA, 2005, p. D-10.
(21) Blume, M.; Orbach, R. Spin-Lattice Relaxation of S -State Ions: Mn 2 + in a Cubic Environment. *Phys. Rev.* **1962**, *127* (5), 1587–1592. https://doi.org/10.1103/PhysRev.127.1587.
(22) Savitsky, A.; Dubinskii, A. A.; Zimmermann, H.; Lubitz, W.; Möbius, K. High-Field Dipolar Electron Paramagnetic Resonance (EPR) Spectroscopy of Nitroxide Biradicals for Determining Three-Dimensional Structures of Biomacromolecules in Disordered Solids. *J. Phys. Chem. B* **2011**, *115* (41), 11950–11963. https://doi.org/10.1021/jp206841v.
(23) Abdullin, D.; Duthie, F.; Meyer, A.; Müller, E. S.; Hagelueken, G.; Schiemann, O. Comparison of PELDOR and RIDME for Distance Measurements between Nitroxides and Low-Spin Fe(III) Ions. *J. Phys. Chem. B* **2015**, *119* (43), 13534–13542. https://doi.org/10.1021/acs.jpcb.5b02118.
(24) Razzaghi, S.; Qi, M.; Nalepa, A. I.; Godt, A.; Jeschke, G.; Savitsky, A.; Yulikov, M. RIDME Spectroscopy with Gd(III) Centers. *J. Phys. Chem. Lett.* **2014**, *5* (22), 3970–3975. https://doi.org/10.1021/jz502129t.
(25) Abdullin, D.; Suchatzki, M.; Schiemann, O. Six-Pulse RIDME Sequence to Avoid Background Artifacts. *Appl Magn Reson* **2022**, *53* (3–5), 539–554. https://doi.org/10.1007/s00723-021-01326-1.
(26) Wautelet, P.; Le Moigne, J.; Videva, V.; Turek, P. Spin Exchange Interaction through Phenylene-Ethynylene Bridge in Diradicals Based on Iminonitroxide and Nitronylnitroxide Radical Derivatives. 1. Experimental Investigation of the Through-Bond Spin Exchange Coupling. *J. Org. Chem.* **2003**, *68* (21), 8025–8036. https://doi.org/10.1021/jo034723n.
(27) Riplinger, C.; Kao, J. P. Y.; Rosen, G. M.; Kathirvelu, V.; Eaton, G. R.; Eaton, S. S.; Kutateladze, A.; Neese, F. Interaction of Radical Pairs Through-Bond and Through-Space: Scope and Limitations of the Point−Dipole Approximation in Electron Paramagnetic

Resonance Spectroscopy. *J. Am. Chem. Soc.* **2009**, *131* (29), 10092–10106. https://doi.org/10.1021/ja901150j.
(28) Tait, C. E.; Neuhaus, P.; Peeks, M. D.; Anderson, H. L.; Timmel, C. R. Transient EPR Reveals Triplet State Delocalization in a Series of Cyclic and Linear π-Conjugated Porphyrin Oligomers. *J. Am. Chem. Soc.* **2015**, *137* (25), 8284–8293. https://doi.org/10.1021/jacs.5b04511.
(29) Constantinides, C. P.; Berezin, A. A.; Manoli, M.; Leitus, G. M.; Bendikov, M.; Rawson, J. M.; Koutentis, P. A. Effective Exchange Coupling in Alternating-Chains of a π-Extended 1,2,4-Benzotriazin-4-Yl. *New J. Chem.* **2014**, *38* (3), 949–954. https://doi.org/10.1039/C3NJ01235B.
(30) Constantinides, C. P.; Carter, E.; Murphy, D. M.; Manoli, M.; Leitus, G. M.; Bendikov, M.; Rawson, J. M.; Koutentis, P. A. Spin-Triplet Excitons in 1,3-Diphenyl-7-(Fur-2-Yl)-1,4-Dihydro-1,2,4-Benzotriazin-4-Yl. *Chem. Commun.* **2013**, *49* (77), 8662. https://doi.org/10.1039/c3cc44899a.
(31) Paillaud, J. L.; Drillon, M.; De Cian, A.; Fischer, J.; Weiss, R.; Villeneuve, G. Radical-Based Ferromagnetic Chain in Yttrium Diphthalocyanine [YPc 2]· CH 2 Cl 2. *Phys. Rev. Lett.* **1991**, *67* (2), 244–247. https://doi.org/10.1103/PhysRevLett.67.244.
(32) Eaton, S. S.; Woodcock, L. B.; Eaton, G. R. Continuous Wave Electron Paramagnetic Resonance of Nitroxide Biradicals in Fluid Solution. *Concepts Magn Reson Part A* **2018**, *47A* (2), e21426. https://doi.org/10.1002/cmr.a.21426.
(33) Mathivathanan, L.; Rogez, G.; Ben Amor, N.; Robert, V.; Raptis, R. G.; Boudalis, A. K. Origin of Ferromagnetism and Magnetic Anisotropy in a Family of Copper(II) Triangles. *Chem. Eur. J.* **2020**, *26* (56), 12769–12784. https://doi.org/10.1002/chem.202001028.
(34) Neuman, N. I.; Burna, E.; Baggio, R.; Passeggi, M. C. G.; Rizzi, A. C.; Brondino, C. D. Transition from Isolated to Interacting Copper(II) Pairs in Extended Lattices Evaluated by Single Crystal EPR Spectroscopy. *Inorg. Chem. Front.* **2015**, *2* (9), 837–845. https://doi.org/10.1039/C5QI00086F.
(35) Lenz, S.; König, D.; Hunger, D.; Slageren, J. Room-Temperature Quantum Memories Based on Molecular Electron Spin Ensembles. *Adv. Mater.* **2021**, *33* (30), 2101673. https://doi.org/10.1002/adma.202101673.
(36) Bowman, M. K.; Krzyaniak, M. D.; Cruce, A. A.; Weber, R. T. Skew Projection of Echo-Detected EPR Spectra for Increased Sensitivity and Resolution. *Journal of Magnetic Resonance* **2013**, *231*, 117–125. https://doi.org/10.1016/j.jmr.2013.03.011.
(37) Lu, J.; Hoehne, F.; Stegner, A. R.; Dreher, L.; Stutzmann, M.; Brandt, M. S.; Huebl, H. High-Resolution Electrical Detection of Free Induction Decay and Hahn Echoes in Phosphorus-Doped Silicon. *Phys. Rev. B* **2011**, *83* (23), 235201. https://doi.org/10.1103/PhysRevB.83.235201.
(38) Slichter, C. P. *Principles of Magnetic Resonance*; Cardona, M., Fulde, P., von Klitzing, K., Queisser, H.-J., Lotsch, H. K. V., Series Eds.; Springer Series in Solid-State Sciences; Springer Berlin Heidelberg: Berlin, Heidelberg, 1990; Vol. 1. https://doi.org/10.1007/978-3-662-09441-9, p. 42-43.
(39) Bowman, M. K.; Maryasov, A. G. The Direct Dimension in Pulse EPR. *Appl Magn Reson* **2021**, *52* (8), 1041–1062. https://doi.org/10.1007/s00723-021-01362-x.
(40) Schweiger, A.; Jeschke, G. *Principles of Pulse Electron Paramagnetic Resonance*; Oxford University Press: Oxford, UK ; New York, 2001, p. 429.

(41) De Raedt, H.; Barbara, B.; Miyashita, S.; Michielsen, K.; Bertaina, S.; Gambarelli, S. Quantum Simulations and Experiments on Rabi Oscillations of Spin Qubits: Intrinsic vs Extrinsic Damping. *Physical Review B* **2012**, *85* (1). https://doi.org/10.1103/PhysRevB.85.014408.

(42) Drew, S. C.; Boas, J. F.; Pilbrow, J. R.; Boyd, P. D. W.; Paul, P.; Reed, C. A. Spin States of C_{60}^{3-} and $C_{120}O^{n-}$ (n = 2, 3, 4) Anions Using Electron Spin Transient Nutation Spectroscopy. *J. Phys. Chem. B* **2003**, *107* (41), 11353–11359. https://doi.org/10.1021/jp035632x.

(43) Eaton, S. S.; Eaton, G. R. Impact of Electron–Electron Spin–Spin Coupling on Electron-Spin Turning Angle in a Spin-Labeled Copper(II) Complex. *Journal of Magnetic Resonance, Series A* **1995**, *117* (1), 62–66. https://doi.org/10.1006/jmra.1995.9972.

(44) Kühne, T. D.; Iannuzzi, M.; Del Ben, M.; Rybkin, V. V.; Seewald, P.; Stein, F.; Laino, T.; Khaliullin, R. Z.; Schütt, O.; Schiffmann, F.; Golze, D.; Wilhelm, J.; Chulkov, S.; Bani-Hashemian, M. H.; Weber, V.; Borštnik, U.; Taillefumier, M.; Jakobovits, A. S.; Lazzaro, A.; Pabst, H.; Müller, T.; Schade, R.; Guidon, M.; Andermatt, S.; Holmberg, N.; Schenter, G. K.; Hehn, A.; Bussy, A.; Belleflamme, F.; Tabacchi, G.; Glöß, A.; Lass, M.; Bethune, I.; Mundy, C. J.; Plessl, C.; Watkins, M.; VandeVondele, J.; Krack, M.; Hutter, J. CP2K: An Electronic Structure and Molecular Dynamics Software Package - Quickstep: Efficient and Accurate Electronic Structure Calculations. *J. Chem. Phys.* **2020**, *152* (19), 194103. https://doi.org/10.1063/5.0007045.

(45) Boudalis, A. K.; Kumar, K. S.; Ruben, M. Molecular Devices. In *Reference Module in Chemistry, Molecular Sciences and Chemical Engineering*; Elsevier, 2021; p B9780081026885001000. https://doi.org/10.1016/B978-0-08-102688-5.00061-1.

(46) Hu, K.-N.; Yu, H.; Swager, T. M.; Griffin, R. G. Dynamic Nuclear Polarization with Biradicals. *J. Am. Chem. Soc.* **2004**, *126* (35), 10844–10845. https://doi.org/10.1021/ja039749a.

(47) Nelson, J. N.; Zhang, J.; Zhou, J.; Rugg, B. K.; Krzyaniak, M. D.; Wasielewski, M. R. CNOT Gate Operation on a Photogenerated Molecular Electron Spin-Qubit Pair. *J. Chem. Phys.* **2020**, *152* (1), 014503. https://doi.org/10.1063/1.5128132.

Table of contents entry